Optomechanical effects in nanocavity-enhanced resonant Raman scattering of a single molecule

Xuan-Ming Shen,[1] Yuan Zhang,[1,*] Shunping Zhang,[2] Yao Zhang,[3] Qiu-Shi Meng,[3] Guangchao Zheng,[4] Siyuan Lv,[5] Luxia Wang,[5] Roberto A. Boto,[6,7] Chongxin Shan,[1,†] and Javier Aizpurua[6,7,‡]

[1]*Henan Key Laboratory of Diamond Optoelectronic Materials and Devices, Key Laboratory of Material Physics, Ministry of Education, School of Physics and Microelectronics, Zhengzhou University, Daxue Road 75, Zhengzhou 450052, China*

[2]*School of Physics and Technology, Center for Nanoscience and Nanotechnology, and Key Laboratory of Artificial Micro- and Nano-structures of Ministry of Education, Wuhan University, Wuhan 430072, China*

[3]*Hefei National Research Center for Physical Sciences at the Microscale and Synergetic Innovation Centre of Quantum Information and Quantum Physics, University of Science and Technology of China, Hefei, Anhui 230026, China*

[4]*School of Physics and Microelectronics, Zhengzhou University, Daxue Road 75, Zhengzhou 450052, China*

[5]*Department of Physics, University of Science and Technology Beijing, 100083 Beijing, China*

[6]*Center for Material Physics (CSIC - UPV/EHU and DIPC), Paseo Manuel de Lardizabal 5, Donostia-San Sebastian Gipuzkoa 20018, Spain*

[7]*Donostia International Physics Center, Paseo Manuel de Lardizabal 4, Donostia-San Sebastian 20018, Spain*

(Received 6 October 2022; revised 6 February 2023; accepted 8 February 2023; published 24 February 2023)

In this paper, we address the optomechanical effects in surface-enhanced resonant Raman scattering (SERRS) from a single molecule in a nanoparticle on mirror (NPoM) nanocavity by developing a quantum master-equation theory, which combines macroscopic quantum electrodynamics and electron-vibration interaction within the framework of open quantum system theory. We supplement the theory with electromagnetic simulations and time-dependent density functional theory calculations in order to study the SERRS of a methylene blue molecule in a realistic NPoM nanocavity. The simulations allow us not only to identify the conditions to achieve conventional optomechanical effects, such as vibrational pumping, nonlinear scaling of Stokes and anti-Stokes scattering, but also to discovery distinct behaviors, such as the saturation of exciton population, the emergence of Mollow triplet side bands, and higher-order Raman scattering. All in all, our study might guide further investigations of optomechanical effects in resonant Raman scattering.

DOI: 10.1103/PhysRevB.107.075435

I. INTRODUCTION

Surface-enhanced Raman scattering (SERS) refers to the enhancement of the Raman signal of molecules located near metallic nanostructures [1]. This effect is partially due to the charge transfer between the molecule and the metal (chemical enhancement [2]) but the main contribution is due to the enhanced electromagnetic field by the metallic nanostructure (electromagnetic field enhancement [3]). Moreover, since Raman enhancement can reach tens of orders of magnitude for molecules near electromagnetic hot spots [4], vibrational pumping associated with the enhanced Stokes scattering can potentially compete with thermal vibrational excitation, and is thus able to introduce nonlinear scaling of anti-Stokes scattering with increasing laser intensity [5–8].

Earlier studies on vibrational pumping were hindered by the difficulty of quantitatively estimating the vibrational pumping rate. To overcome this problem, in recent years, Schmidt *et al.* [9] and Roelli *et al.* [10] were inspired by cavity optomechanics [11], and developed a molecular optomechanics theory [12] for off-resonant Raman scattering. According to this theory, molecular vibrations interact with the plasmonic response of metallic nanostructures through optomechanical coupling, and the vibrational pumping rate can be quantitatively determined by this coupling together with the molecular vibrational energy and the plasmonic response (such as mode energy, damping rate, and laser excitation). Aside from vibrational pumping, molecular optomechanics also allows us to investigate many novel effects, such as nonlinear divergent Stokes scattering (known as parametric instability in cavity optomechanics [11]), collective optomechanical effects [13], higher-order Raman scattering [14], and optical spring effect [15] among others.

Metallic nanocavities, formed by metallic nanoparticle dimers [16], metal nanoparticle on mirror (NPoM) [17] or STM tip-on-metallic substrate [18], are ideal configuration for observation of novel optomechanical effects in experiments because they provide hundredfolds of local field enhancement inside the nanogaps, and thus provide easily SERS enhancement over 10^{12}. Using biphenyl-4-thiol molecules inside NPoM gold nanocavities, Benz, *et al.* [19] observed nonlinear scaling of anti-Stokes SERS with increasing continuous-wave (cw) laser excitation (thus justifying vibrational pumping). Later on, using the same system, nonlinear scaling of Stokes SERS was observed for pulsed laser illumination of much stronger intensity at room temperature [20] (proving the precursor of parametric instability and the collective optomechanical effect). Recently, Xu *et al.* [21] observed also the

*yzhuaudipc@zzu.edu.cn
†cxshan@zzu.edu.cn
‡aizpurua@ehu.es

similar nonlinear Stokes SERS with a MoS_2 monolayer within metallic nanocube-on-mirror nanocavities.

Most of the studies on molecular optomechanics so far focus on the off-resonant Raman scattering. Because this scattering is usually weak, the observation of its optomechanical effects requires normally very strong laser excitation. To reduce the required laser intensity, in this paper, we propose to combine the metallic nanocavities with the molecular resonant effect to enhance the Raman scattering of molecules. The molecular resonant effect refers to the enhancement of the Raman scattering when the laser is resonant with molecular electronic excited states. Indeed, the earliest studies on vibrational pumping focused on surface-enhanced resonant Raman scattering (SERRS) of dye molecules [5–8] (such as crystal violet, or rhodamine 6G).

In our previous works [22,23], we extended the molecular optomechanics approach based on single plasmon mode to SERRS, and showed that the electron-vibration coupling, leading to resonant Raman scattering, resembles the plasmon-vibration optomechanical coupling, and thus we show that optomechanical effects can also occur in resonant Raman scattering. Moreover, since the former coupling is usually much larger, and the electronic excitation is usually much narrower than the plasmon excitation, optomechanical effects in SERRS can potentially occur for much smaller laser intensities. Furthermore, in our other works [15,24], we showed that the plasmonic response of metallic nanocavities is far more complex than that of a single mode, and the molecular optomechanics is strongly affected by the plasmonic pseudomode, formed by the overlapping higher-order plasmonic modes [25].

To address SERRS from molecules in realistic metallic nanocavities, here we develop a theory that combines the macroscopic quantum electrodynamics description [26,27] with the electron-vibration interaction, and derive a quantum master equation for the molecular electronic and vibrational dynamics. As an example, we apply our theory to a single methylene blue molecule inside a gold NPoM nanocavity, as shown in Fig. 1. To maximize the molecule-nanocavity interaction, we assume that the molecule is encapsulated by a cucurbit[n] cage [28] so that it stands vertically.

Our study shows that most of the optomechanical effects, such as vibrational pumping, parametric instability, vibrational saturation, Raman line shift and narrowing, and so on, can occur in SERRS at lower laser intensity threshold. However, the molecular excitation saturates for strong laser excitation because of its two-level fermionic nature (in contrast to the infinite levels of a bosonic plasmon), and the SERRS signal saturates and even vanishes for strong laser excitation. In addition, we also find that the resonant fluorescence is redshifted by about 40 meV (plasmonic Lamb shift [29,30]), and broadened by about 22 meV (due to the Purcell effect), and also shows three broad peaks for strong laser excitation [31] (corresponding to the Mollow triplet similar to the situation in quantum optics [32]).

Our paper is organized as follows. We present first our theory for SERRS of single molecule in plasmonic nanocavities in Sec. II, which is followed by the time-dependent density functional theory (TDDFT) calculation of the methylene blue molecule in Sec. III and the electromagnetic simulation of the NPoM nanocavity in Sec. IV. In Sec. V, we study the evolution of the SERRS and fluorescence with increasing laser illumination, which is zero, blue, or red detuned with respect to the molecular excitation, respectively. In the end, we conclude our work and comment on the extensions in the future.

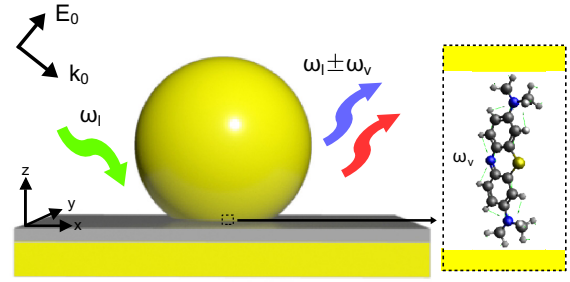

FIG. 1. A vertically orientated methylene blue molecule (with black, white, blue, yellow spheres for carbon, hydrogen, nitrogen, sulfur atoms, respectively) in the middle of a nanoparticle on mirror (NPoM) nanocavity of 0.9 nm thick, formed by a truncated gold sphere with a 40-nm diameter and a bottom facet of a 10-nm diameter on top of a flat gold substrate. The laser excitation of frequency ω_l is enhanced in the nanocavity, and the enhanced local field excites the molecule vibrating with frequency ω_v. The emitted field at frequency ω_l (Rayleigh scattering) and at frequencies $\omega_l - \omega_v, \omega_l + \omega_v$ (Stokes and anti-Stokes scattering), as well as frequencies independent of ω_l (fluorescence), is enhanced and propagated to the far field.

II. QUANTUM MASTER EQUATION

To address the processes shown in Fig. 1, we have developed a theory that combines macroscopic quantum electrodynamics and electron-vibration interaction. In Appendix A, we detail the treatment of the interaction between a single molecule and the plasmonic (electromagnetic) field of the metallic nanocavity. To reduce the degrees of freedom, we apply the open quantum system theory [33] where we consider the plasmonic field as a reservoir and treat the molecule-plasmonic field interaction as a perturbation in second order, to finally achieve an effective master equation for the single molecule. Here, this treatment is valid since the single molecule couples relatively weakly with the nanocavity. However, further consideration is required for the system with more molecules, which might enter into the strong coupling regime [28].

To account for other mechanisms, like the molecular vibrations and the molecular excitation, we generalize the effective master equation to obtain

$$\begin{aligned}\frac{\partial}{\partial t}\hat{\rho} = &-\frac{i}{\hbar}[\hat{H}_{\rm ele} + \hat{H}_{\rm las} + \hat{H}_{\rm vib} + \hat{H}_{\rm ele\text{-}vib} + \hat{H}_{\rm pla}, \hat{\rho}] \\ &+ (\Gamma + \gamma_e)\mathcal{D}_{\hat{\sigma}}[\hat{\rho}] + \frac{\chi_e}{2}\mathcal{D}_{\hat{\sigma}^z}[\hat{\rho}] \\ &+ \sum_\nu \gamma_\nu \left\{ \left(n_\nu^{\rm th} + 1\right)\mathcal{D}_{\hat{b}_\nu}[\hat{\rho}] + n_\nu^{\rm th}\mathcal{D}_{\hat{b}_\nu^\dagger}[\hat{\rho}] \right\}. \end{aligned} \tag{1}$$

In the above equation, we treat the molecular electronic ground and excited states as a two-level system, and specify its Hamiltonian as $\hat{H}_{\rm ele} = \hbar(\omega_e/2)\hat{\sigma}^z$ with transition frequency

ω_e and Pauli operator $\hat{\sigma}^z$. We treat the molecular excitation semiclassically with the Hamiltonian $\hat{H}_{\rm las} = \hbar(\hat{\sigma}^\dagger v e^{-i\omega_{\rm las}t} + v^* e^{i\omega_{\rm las}t}\hat{\sigma})$, where the molecule near-field coupling $\hbar v = -\mathbf{d}_m \cdot \mathbf{E}(\mathbf{r}_m, \omega_{\rm las})$ is determined by the enhanced local electric field $\mathbf{E}(\mathbf{r}_m, \omega_{\rm las})$ at the molecular position $\mathbf{r}_m$, activated by a laser with frequency $\omega_{\rm las}$. Here, $\hat{\sigma}^\dagger$, $\hat{\sigma}$ are the raising and lowering operators of the molecular excitation. We approximate the molecular vibrations as quantized harmonic oscillators and specify their Hamiltonian $\hat{H}_{\rm vib} = \hbar\sum_\nu \omega_\nu \hat{b}_\nu^\dagger \hat{b}_\nu$ with the frequency ω_ν, the creation $\hat{b}_\nu^\dagger$ and annihilation $\hat{b}_\nu$ operators of the νth vibrational mode. The electron-vibration interaction takes the form $\hat{H}_{\text{ele-vib}} = \hbar\sum_\nu \omega_\nu d_\nu \hat{\sigma}^\dagger\hat{\sigma}(\hat{b}_\nu^\dagger + \hat{b}_\nu)$ with the dimensionless displacement $d_\nu = \sqrt{S_\nu}$ (S_ν is known as the Huang-Rhys factor [34]) of the parabolic potential energy surface for the electronic ground and excited states. Here, the electronic transition frequency ω_e has already accounted for the shift $\sum_\nu d_\nu\omega_\nu$ due to the electron-vibration coupling.

The elimination of the plasmonic field leads to one Hamiltonian $\hat{H}_{\rm pla} = \hbar(\Omega/2)\hat{\sigma}^z$ and one Lindblad term $\Gamma\mathcal{D}_{\hat{\sigma}}[\hat{\rho}]$ with the superoperator $\mathcal{D}_{\hat{o}}[\hat{\rho}] = \hat{o}\hat{\rho}\hat{o}^\dagger - \frac{1}{2}\hat{o}^\dagger\hat{o}\hat{\rho} - \frac{1}{2}\hat{\rho}\hat{o}^\dagger\hat{o}$ (for any operator $\hat{o}$), which describe the shift

$$\Omega = -\frac{1}{\hbar\epsilon_0}\frac{\omega_e^2}{c^2}\mathbf{d}_m \cdot \mathrm{Re}\overleftrightarrow{G}(\mathbf{r}_m, \mathbf{r}_m; \omega_e)\cdot\mathbf{d}_m^* \tag{2}$$

of the transition frequency (plasmonic Lamb shift [29,30]), and the Purcell-enhanced decay rate

$$\Gamma = \frac{2}{\hbar\epsilon_0}\frac{\omega_e^2}{c^2}\mathbf{d}_m \cdot \mathrm{Im}\overleftrightarrow{G}(\mathbf{r}_m, \mathbf{r}_m; \omega_e)\cdot\mathbf{d}_m^* \tag{3}$$

of the molecule. Here, ϵ_0 and c are the vacuum permittivity and the speed of light, and $\mathbf{d}_m$ is the molecular transition dipole. $\overleftrightarrow{G}(\mathbf{r}, \mathbf{r}'; \omega)$ is the dyadic Green's function, which connects usually the electric field with frequency ω at the position $\mathbf{r}$ with the dipole point source at another position $\mathbf{r}'$ in classical electrodynamics. The remaining terms of Eq. (1) describe the dissipation of the electronic states, including the nonradiative decay $\gamma_e\mathcal{D}_{\hat{\sigma}}[\hat{\rho}]$ with a rate γ_e, and the dephasing $\frac{\chi_e}{2}\mathcal{D}_{\hat{\sigma}^z}[\hat{\rho}]$ with a rate χ_e, and the thermal decay and pumping of the vibrational modes $\sum_\nu\{\gamma_\nu(n_\nu^{\rm th}+1)\mathcal{D}_{\hat{b}}[\hat{\rho}] + \gamma_\nu n_\nu^{\rm th}\mathcal{D}_{\hat{b}^\dagger}[\hat{\rho}]\}$ with a rate γ_ν, where $n_\nu^{\rm th} = [\exp\{\hbar\omega_\nu/k_BT\} - 1]^{-1}$ is the thermal vibrational population at temperature T (k_B is Boltzmann constant).

In Appendix B, we have derived the formula to compute the spectrum $dW(\omega)/d\Omega$ measured by a detector in the far field:

$$\frac{dW}{d\Omega}(\omega) \approx K(\omega)\mathrm{Re}\int_0^\infty d\tau\, e^{i\omega\tau}\mathrm{tr}\{\hat{\sigma}\hat{\varrho}(\tau)\}. \tag{4}$$

In this equation, the propagation factor is defined as

$$K(\omega) = \frac{\hbar^2 c r^2}{4\pi^2\epsilon_0}\left|\frac{\omega^2}{c^2}\overleftrightarrow{G}(\mathbf{r}_d, \mathbf{r}_m; \omega)\cdot\mathbf{d}_m^*\right|^2, \tag{5}$$

where the dyadic Green's function $\overleftrightarrow{G}(\mathbf{r}_d, \mathbf{r}_m; \omega)$ connects the electric field at frequency ω at position $\mathbf{r}_d$ of the detector with the molecule at the position $\mathbf{r}_m$. r denotes the distance between the molecule and the detector. In addition, the operator $\hat{\varrho}(\tau)$ satisfies the same master equation (1) as $\hat{\rho}$, but with initial condition $\hat{\varrho}(0) = \hat{\rho}\hat{\sigma}^\dagger$.

To solve the master equation (1), we introduce the density matrix $\rho_{an,bm}$ (with $a, b = g, e$) in the basis of the product states $\{|e\rangle|m\rangle, |g\rangle|n\rangle\}$, where $|e\rangle$, $|g\rangle$ denote the electronic excited and ground state of the molecule, and $|m\rangle = \prod_\nu|m_\nu\rangle$, $|n\rangle = \prod_\nu|n_\nu\rangle$ are the occupation number states of the vibrational modes (m_ν, n_ν are positive integers). From Eq. (1), we can easily derive the equation for the density matrix. In this study, we utilize the QUTIP toolkit [35,36] to solve the density matrix equation, and then determine the electronic excited-state population $\langle\hat{\sigma}^\dagger\hat{\sigma}\rangle = \mathrm{tr}\{\hat{\sigma}^\dagger\hat{\sigma}\hat{\rho}\}$, the mean vibrational population $\langle\hat{b}_\nu^\dagger\hat{b}_\nu\rangle = \mathrm{tr}\{\hat{b}_\nu^\dagger\hat{b}_\nu\hat{\rho}\}$, the two-time correlation $C(\tau) \equiv \mathrm{tr}\{\hat{\sigma}\hat{\varrho}(\tau)\}$, and the spectrum $dW(\omega)/d\Omega$.

In the weak-excitation limit $\langle\hat{\sigma}^\dagger\hat{\sigma}\rangle \ll 1$, we can apply the Holstein-Primakoff approximation [37] to the molecule by introducing the bosonic creation $\hat{a}$ and annihilation operator $\hat{a}^\dagger$ such that $\hat{\sigma}^z \equiv 2\hat{a}^\dagger\hat{a} - 1$, $\hat{\sigma}^\dagger \equiv \hat{a}^\dagger\sqrt{1-\hat{a}^\dagger\hat{a}} \approx \hat{a}^\dagger$, $\hat{\sigma} \equiv \sqrt{1-\hat{a}^\dagger\hat{a}}\hat{a} \approx \hat{a}$. In this case, we can carry out the replacement $\hat{\sigma}^z \to \hat{a}^\dagger\hat{a}$, $\hat{\sigma}^\dagger \to \hat{a}^\dagger$, $\hat{\sigma} \to \hat{a}$ in the master equation (1), and then obtain the equation equivalent to the one used in the molecular optomechanics theory [9,10]. This indicates that in the current situation the molecular excitation works effectively as the plasmon mode, and the electron-vibration coupling as the optomechanical coupling, i.e., $g_\nu = \omega_\nu d_\nu$. Thus, we expect to find many interesting optomechanical effects in the current system, namely, vibrational pumping, nonlinear Raman scattering, Raman line shift and broadening [13], and so on. For typical values of $\hbar\omega_\nu = 200$ meV and $d = 0.1$, we obtain $\hbar g_\nu = 20$ meV, which is about two orders of magnitude larger than in typical molecular optomechanics [9,13]. Thus, we expect to observe a variety of optomechanical effects in SERRS with, however, lower laser intensity threshold.

III. ELECTRONIC AND VIBRATIONAL ANALYSIS OF METHYLENE BLUE MOLECULE

To apply the theory developed in the previous section, we carry out electronic and vibrational excitation analysis for the methylene blue molecule with the use of the GAUSSIAN 16 package, the cam-B3LYP hybrid functional, and 6-311$g(d, p)$ basis set (Fig. 2). First, we carry out density functional theory (DFT) calculations to optimize the molecule, compute the vibrational modes for the electronic ground state, and extract their equilibrium normal-mode coordinates Q_ν. Second, we carry out time-dependent DFT (TDDFT) calculations to optimize the molecule on the first excited state, compute the vibrational modes for this state, and extract the corresponding equilibrium normal-mode coordinates Q'_ν. From these calculations, we can also determine the transition energy $\hbar\omega_e$, and the transition dipole moment $\mathbf{d}_m$ for the maximal emission (in the Tamm-Dancoff approximation [38]). Finally, we compute the vibronic spectrum for one-photon emission using the Franck-Condon approach [39], and extract the displacement matrix K in the Duschinsky transformation [40] $Q'_\nu = JQ + K$ (with J matrix representing the normal-mode mixing during the transition). The Huang-Rhys factors can be computed according to the relationship $S_\nu = (4\pi^2\omega_\nu c/2h)K_\nu^2$. In the DFT and TDDFT calculations, we consider the methylene blue molecule alone because the cucurbit cage does not have absorption in the UV-visible range, and does not affect the fluorescence of the molecule (see Fig. 2 and Fig. S1d of

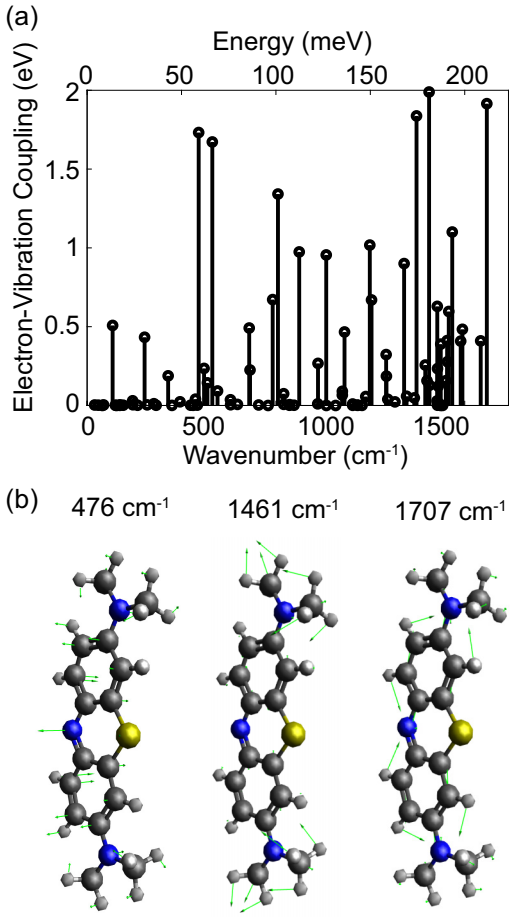

FIG. 2. Electronic and vibrational calculation of the methylene blue molecule. (a) Electron-vibration coupling versus wave number (lower axis) and energy (upper axis) of the vibrational modes. (b) Vibrational patterns of the 476-cm^{-1}(left), 1461-cm^{-1} (middle), and 1707-cm^{-1} (right) vibrational modes of the same molecule.

Ref. [28]). Furthermore, since the cucurbit cage has more than 84 atoms, the TDDFT calculations of the molecule plus the cucurbit cage will be extremely time consuming.

From the above calculations, we obtain the transition energy $\hbar\omega_e \approx 2.88$ eV, which is consistent with the result in [41] but higher than the energy of the emission maximum 1.82 eV (wavelength of 680 nm). The transition dipole moment obtained is $|\mathbf{d}_m| \approx 11$ Debye (along the long molecular axis) for the methylene blue molecule, which agrees with the result in Ref. [41] but is larger than the values $2.55 \sim 4.23$ Debye in Ref. [42]. Figure 2(a) shows the computed electron-vibration coupling in the order of eV versus the wave number of vibrational modes. This coupling is strong for the vibrational modes around 500, 1400, and 1700 cm^{-1}, and this characteristic is similar to that of the observed SERRS of the same molecule in experiments (see Fig. S11 in Ref. [28]). Figure 2(b) shows the vibrational pattern for the 476-cm^{-1} (left), 1461-cm^{-1} (middle), and 1707-cm^{-1} (right) mode, which can be assigned to the N-C swing mode, the CH_3-rocking mode, and the C = C stretching mode, respectively. The electron-vibration coupling for these modes is estimated as $\hbar\omega_v d_v = 1.732$, 1.989, and 1.915 eV from Fig. 2(a).

The overestimation of the excitation energy is due to the limit of the TDDFT to describe π-conjugated systems [42], and thus the calculated geometry of excited state might be also unreliable. Since the Huang-Rhys factor or the electron-vibration coupling is calculated from the geometry difference of the electronic ground and excited states, the unreliable excited-state geometry might lead to the overestimation of this factor. Furthermore, we consider the methylene blue molecule in vacuum when carrying out the geometry optimization, but the solvent around the molecule might affect the geometry and thus the electron-vibration coupling. By using the advanced method, such as configuration of interactions, and accounting for the solvent effect, we might improve the calculation of the excitation energy and the electron-vibration coupling. However, because these calculations are extremely time consuming, and beyond the focus of our study, we have decided to modify these parameters based on what reported in literature. In the following simulations, we choose electronic transition energy $\hbar\omega_e = 1.82$ eV as measured in the experiment, and a transition dipole moment $|\mathbf{d}_m| \approx 3.8$ Debye (compromised value among different calculations), and downscale the electron-vibration coupling to the typical values $\hbar\omega_v d_v = 17.3, 19.9, 19.2$ meV for the 476-, 1461-, and 1707-cm^{-1} mode (scaled down by a factor 100 to reach the typical values), respectively.

IV. ELECTROMAGNETIC RESPONSE OF THE NPOM NANOCAVITY

The considered NPoM nanocavity is specified in Fig. 1, and consists of a gold nanosphere with 40-nm diameter on a gold film. The nanosphere is truncated at bottom with a fact of 10-nm diameter, and is separated from the film by 0.9 nm. For the electromagnetic simulations, we utilize the boundary element method (BEM) method [43,44] as implemented in the metal nanoparticle BEM toolkit [45,46], and use the gold dielectric function as determined in the experiment [47], and assume the dielectric permittivity 2.1 for the nanogap. First, we illuminate the system by a *p*-polarized plane wave within a wavelength range [500,1000] nm with an incident angle of 55° to the surface normal, and compute the near-field enhancement of the vertical field component $|E_z/E_0|$ in the middle of the nanocavity [blue solid line in Fig. 3(a)]. The field enhancement shows two peaks with maxima about 400 and 100 at around 685 and 580 nm, which are attributed to the bonding dipole plasmon (BDP) and the bounding quadrupole plasmon (BQP), respectively [19,20,24]. In addition, we observe also two peaks at similar wavelengths in the far-field scattering spectrum (not shown).

Second, we illuminate the system with a point dipole located in the middle of the NPoM nanocavity, then compute the scattered electric field at the position of the dipole, and finally compute the scattered dyadic Green's function as the ratio of the scattered field and the dipole amplitude [24]. On the right axis of Fig. 3(a), we show the real (red dashed line) and imaginary (green dotted line) parts of the *zz* component of the dyadic Green's tensor in such situation. The imaginary part shows two peaks at similar wavelengths as for the near-field enhancement, but also one extra peak at around 520 nm, which can be attributed to the plasmon pseudomode arising

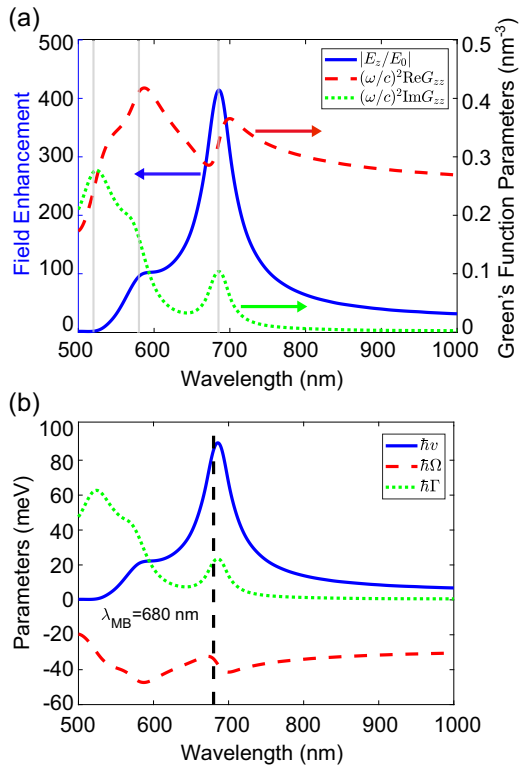

FIG. 3. Plasmonic response of the NPoM nanocavity. (a) Near-field enhancement (blue solid line, left axis), real part (red dashed line) and imaginary part (green dotted line) of the scattered dyadic Green's function (right axis) for a dipole in the middle of the nanocavity, where the vertical gray lines from right to left show the wavelengths of 685, 580, and 520 nm, respectively. (b) Molecule near-field coupling $\hbar|v|$ (blue solid line) for laser intensity 10^4 μW/μm^2 versus the laser wavelength, Lamb shift $\hbar\Omega$ (red dashed line), and Purcell-enhanced decay rate $\hbar\Gamma$ (green dotted line) versus the wavelength. Here, the molecule is assumed to stand vertically and the transition dipole is 3.8 Debye, and the vertical dashed line indicates the transition wavelength $\lambda_e = 680$ nm of the methylene blue molecule. For more details, see the text.

from the overlapped higher-order plasmon modes [25]. In that figure, we also see two Fano features around the wavelengths of the BDP and BQP modes in the real part of the dyadic Green's function. Note that the real part is always positive. As shown in our previous studies [24], the general wavelength dependence of the dyadic Green's function resembles that of the metal-insulator-metal structure (for the same metal, same dielectric, and same thickness as the NPoM gap), which can be attributed to the resemblance of the NPoM mode with the guiding surface plasmon modes and the high-momentum surface-wave modes [48].

Assuming that the molecular transition dipole is 3.8 Debye (typical value for the methylene blue molecule), we have computed and shown in Fig. 3(b) the molecule near-field coupling $\hbar v$ for laser intensity $I_{\mathrm{las}} = 10^4$ μW/μm^2 (blue solid line), i.e., a value achievable in experiment [20], the plasmonic Lamb shift $\hbar\Omega$ (red dashed line), and the Purcell-enhanced spontaneous emission rate Γ (green dotted line). $\hbar v$ follows the shape of the near-field enhancement, and reaches the maximal value around 80 meV for the laser resonant with the BDP mode, i.e., $\lambda_{\mathrm{las}} \approx \lambda_{\mathrm{BDP}}$. $\hbar\Omega$ follows the shape of the real part of the dyadic Green's function (with a sign change), and changes in the range of [−20 meV, −50 meV]. $\hbar\Gamma$ follows the shape of the imaginary part of the dyadic Green's function, and varies in the range of [0, 60 meV]. For the methylene blue molecule with the transition wavelength $\lambda_e = 680$ nm, we obtain $\hbar v \approx 80$ meV, $\hbar\Omega \approx -40$ meV, and $\hbar\Gamma \approx 22$ meV. Since these parameters (and also the molecular intrinsic decay rate) are of the same order of magnitude, we expect that the molecule in the NPoM nanocavity can reach the nonlinear regime with the typical laser intensities used in experiments.

V. SERRS RESPONSE TO LASER EXCITATION

We are now in the position to study the SERRS response of the methylene blue molecule in the NPoM nanocavity to the laser excitation. As explained in the end of Sec. II, the theory for SERRS resembles that of molecular optomechanics in the low excitation limit, and thus we expect a different response for laser excitation which is resonant, and blue and red detuned with respect to the molecular excitation, similar to the situations in molecular optomechanics [13]. Thus, in the following, we analyze the SERRS response in the three cases.

In our simulations, we consider the laser intensity up to 10^5 μW/μm^2. In the experiment, the laser intensity up to 10^4 μW/μm^2 can be achieved with the cw laser, and the one with up to 10^5 μW/μm^2 can be achieved with the picosecond pulsed laser (see Figs. 3 and 4 of Ref. [20]). While the strong cw laser might affect the geometry of the nanocavity and damage the molecular sample due to the accumulated heating, the picosecond pulsed laser can avoid these side effects by reducing dramatically the accumulated heating, and thus would be recommended for the effects as revealed below. In Fig. 10 of Appendix C, we have studied the system response under the picosecond pulsed laser illumination by introducing a time-dependent molecule near-field coupling.

A. Resonant laser excitation

We study the SERRS response for continuous laser illumination of increasing intensity I_{las}, which is resonant with the molecular excitation. Figure 4(a) shows that for I_{las} smaller than 10^3 μW/μm^2, the excited-state population $\langle\hat{\sigma}^\dagger\hat{\sigma}\rangle$ increases first monotonously from zero, and then saturates at some finite values (dashed lines). For much larger I_{las}, the population shows oscillatory behavior before reaching the saturation value, and the Rabi oscillations become faster with increasing I_{las}. In addition, the saturated value also increases with increasing I_{las}, and eventually becomes close to 0.5. These results indicate that for sufficiently large I_{las}, the coherent excitation of the molecule overcomes the intrinsic and Purcell-enhanced decay rates, and the molecule is driven to a superposition state of the electronic ground and excited states during the oscillatory period, reaching eventually to a mixed steady state.

Figure 4(b) shows that for $I_{\mathrm{las}} \leqslant 10^3$ μW/μm^2, the vibrational population $\langle\hat{b}_\nu^\dagger\hat{b}_\nu\rangle$ increases monotonously with time from the thermal value $n_\nu^{th} = 2.29 \times 10^{-4}$ (at room temperature), and finally saturates at some finite value. The starting time for the rising of the vibrational population decreases with

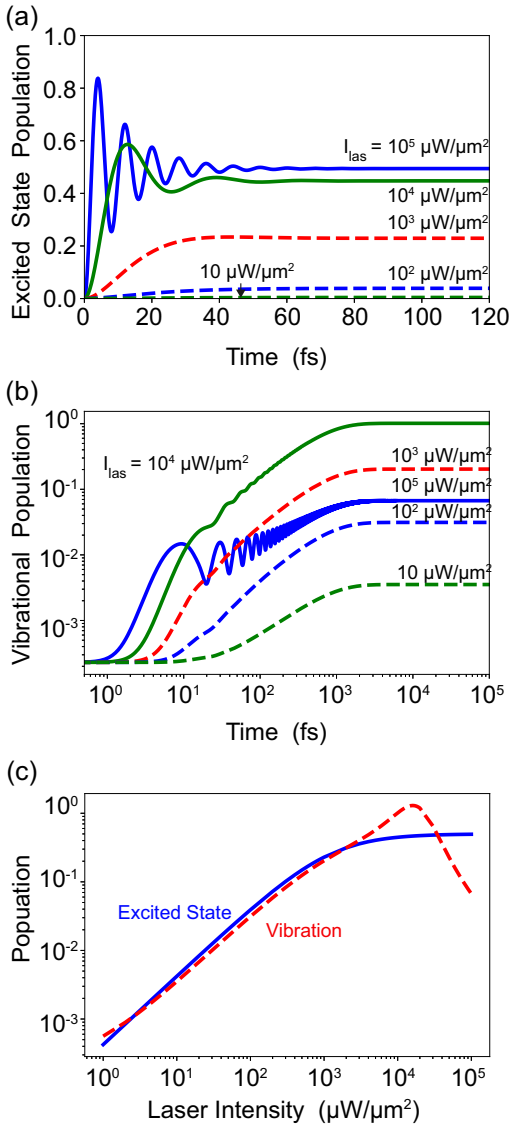

FIG. 4. Electronic and vibrational response to $\lambda_{las} = 693$ nm laser illumination with increasing intensity I_{las}, which is resonant to the Lamb-shifted molecular excitation and switched on abruptly at time zero. (a), (b) Dynamics of the electronic excited-state population $\langle\hat{\sigma}^\dagger\hat{\sigma}\rangle$ (a) and vibrational population $\langle\hat{b}_\nu^\dagger\hat{b}_\nu\rangle$ (b). (c) Evolution of the quantities in (a) and (b) at the steady state with increasing I_{las}. Here, we consider the 1707-cm^{-1} vibrational mode (with energy $\hbar\omega_\nu \approx 211.6$ meV), which leads to a thermal population $n_\nu^{th} = 2.29 \times 10^{-4}$ at room temperature $T = 293$, and assume the electron-vibration coupling $\hbar\omega_\nu d_\nu \approx 19.2$ meV, the intrinsic excitonic decay rate $\hbar\gamma_e = 56.89$ meV, the vanishing dephasing rate $\hbar\chi_e = 0$, and the intrinsic vibrational decay rate $\hbar\gamma_\nu = 1$ meV. For more information, see the text.

increasing I_{las}, and the saturation value increases. For much larger I_{las}, the vibrational population shows some oscillations before reaching the saturation values. As I_{las} increases, the oscillation becomes more pronounced, and the final saturated value decreases. The time to reach the saturated vibrational population is similar for all the laser intensities. Since the saturated values are much larger than the thermal value $n_\nu^{th} \approx 2.26 \times 10^{-4}$, the laser illumination can pump significantly the molecular vibration via the electronic excitation.

The above results demonstrate the transient dynamics of the excited state and vibrational population. In the following, we summarize the influence of the laser intensity on these populations for the system at the steady state [Fig. 4(c)]. We can observe that as I_{las} increases the electronic excited-state population (blue solid line) increases first linearly from zero for $I_{las} \leqslant 10^2$ μW/μm^2, then sublinearly for $I_{las} \leqslant 10^4$ μW/μm^2 and finally saturates at value around 0.5 for $I_{las} \leqslant 10^5$ μW/μm^2. In contrast, the vibrational population (red dashed line) increases firstly sub-linearly for $I_{las} \leqslant 10$ μW/μm^2 (due to the competition with the thermal excitation), linearly for $I_{las} \leqslant 10^3$ μW/μm^2 (due to the vibrational pumping), then sublinearly again for $I_{las} \leqslant 10^4$ μW/μm^2, and finally it gets dramatically decreased for $I_{las} \leqslant 10^5$ μW/μm^2 (due to the saturation of the molecular excitation). The above results indicate that the electronic and vibrational dynamics are within tens of femtosecond and picosecond, respectively. Thus, these dynamics would be modified under the picosecond laser pulse illumination, as shown in Figs. 10(a) and 10(b) of Appendix C.

After understanding the evolution of population, we now consider the response of the SERRS spectrum, as shown in Fig. 5. Figure 5(a) shows that the two-time correlation $C(\tau)$ behaves similarly as the excited-state population (as expected from the quantum regression theorem) except that it starts initially from the excited-state population at the steady state, i.e., $C(0) = \mathrm{tr}\{\hat{\sigma}^\dagger\hat{\sigma}\,\hat{\rho}_{ss}\} = \langle\hat{\sigma}^\dagger\hat{\sigma}\rangle$ (with the steady-state density operator $\hat{\rho}_{ss}$). Applying the Fourier transform to the correlation and weighting the results with the propagation factor according to Eq. (4), we obtain the spectra shown in Fig. 5(b). Here, we have removed the sharp line at the laser wavelength λ_{las} due to the elastic Rayleigh scattering. All the spectra show a broad fluorescence peak at around 690 nm, which is about 12 nm redshifted from the molecular fluorescence peak in free space (black solid line), due to the plasmonic Lamb shift. For larger laser intensity $I_{las} \geqslant 10^3$ μW/μm^2, this peak becomes much broader, and the fluorescence also shows two side peaks at shorter and longer wavelengths. We attribute these three peaks to the typical structure of a Mollow triplet [32], and the two side peaks to the molecule-laser (or plasmon) dressed states. For laser intensity $I_{las} \leqslant 10^4$ μW/μm^2, we observe also three sharp lines at around 619, 785, and 907 nm, which are due to the anti-Stokes, first-order Stokes, and second-order Stokes scattering, respectively. The first-order Stokes line is much stronger than the fluorescence peak and the anti-Stokes line for the smallest I_{las}. However, with increasing I_{las}, this line is overtaken first by the fluorescence peak, and then by the anti-Stokes line. In addition, the second-order Stokes line gets smaller, and eventually vanishes with respect to the broad fluorescence for increasing I_{las}. Notice that the peak around 580 nm is due to the radiation of the BQP mode.

The above results indicate that the two-time correlation function, where one time is fixed at the steady state, has a dynamic within hundreds of femtosecond, and thus the features in the resulting spectrum might be affected by the pulsed laser illumination. To investigate this, we have calculated the more general two-time correlation function, where both the time arguments are varied, and then carried out the Fourier transform to the first time argument, and integrated the resulted transient spectra with respect to the second time

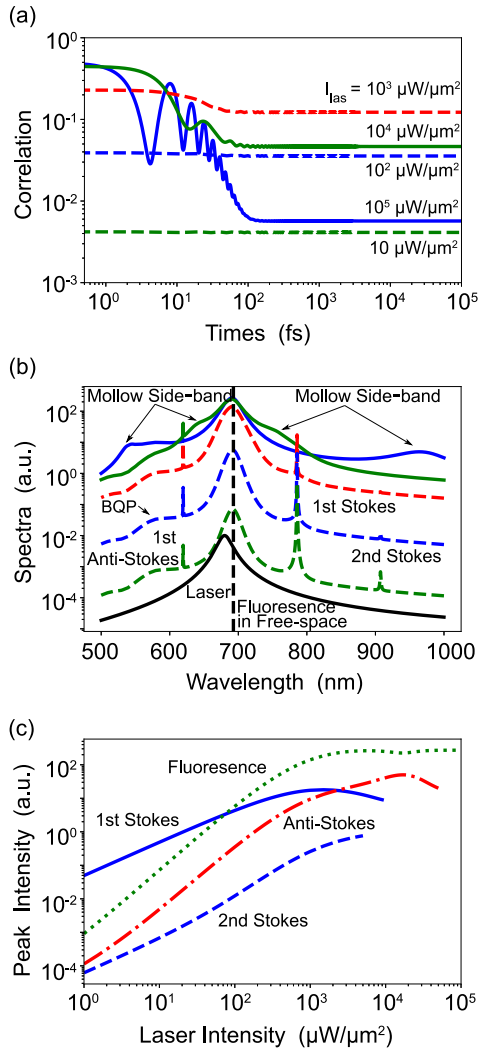

FIG. 5. SERRS response to $\lambda_{las} = 693$ nm laser illumination with increasing intensity I_{las}, resonant to the Lamb-shifted molecular excitation, which is switched on abruptly at time zero. (a) Dynamics of the two-time correlation function $C(\tau)$, and (b) SERRS spectra for $I_{las} = 10, 10^2, 10^3, 10^4, 10^5$ μW/μm^2 [lower to upper curves following the same color code as in (a)], together with molecular fluorescence in free space (black solid line). (c) Evolution of the second- and first-order Stokes line (blue dashed and solid line), and the anti-Stokes line (red dashed-dotted line), as well as the fluorescence peak (green dotted line) with increasing I_{las}. In (b) the Rayleigh scattering line at λ_{las} is removed. Other parameters are the same as in Fig. 4.

argument. As shown in Figs. 10(c) and 10(d) of Appendix C, the calculated spectra are similar to Fig. 5(b) except that the anti-Stokes lines are relatively weaker and the second Stokes lines are invisible, which can be attributed to the relatively weak vibrational pumping under the pulsed excitation.

Furthermore, in Fig. 5(c), we investigate the fluorescence maximum (the green dotted line) and the Raman lines (other lines) as a function of laser intensity I_{las}. We see that the fluorescence maximum follows the trend of the excited-state population as described in Fig. 4(c), and the anti-Stokes line (red dashed-dotted line) follows that of the vibrational population. Both show superlinear scaling for $I_{las} \leqslant 10^3$ μW/μm^2. In contrast, the first- and second-order Stokes lines (blue solid and dashed line) show linear scaling for $I_{las} \leqslant 10^2$ μW/μm^2. For much larger I_{las}, the former shows sublinear scaling, saturation, and finally reduction, while the latter shows the evolution from superlinear to linear, and then to sublinear. In addition, two critical laser intensities appear to be relevant in the evolution of the spectral peaks: the first-order Raman line is equally strong as the fluorescence at about 10^2 μW/μm^2, and as the anti-Stokes line at 2×10^3 μW/μm^2. Interestingly, for $I_{las} \geqslant 10^4$ μW/μm^2, we can still observe the anti-Stokes line but not the Stokes line.

In Figs. 8(a) and 8(b) of Appendix C, we have further examined the evolution of the Raman line shape, and found that the Raman shift does not change so much while the Raman linewidth gets slightly broader for larger I_{las}. In addition, the second-order Stokes line is about twice broader as a compared to the first-order Stokes line.

B. Blue-detuned laser excitation

We now discuss the system response for $\lambda_{las} = 654$ nm laser illumination with increasing intensity I_{las}, which is blue detuned with respect to the Lamb-shifted molecular transition. In Figs. 9(a) to 9(c) of Appendix C, we show that the electronic excited-state population $\langle \hat{\sigma}^\dagger \hat{\sigma} \rangle$, the vibrational population $\langle \hat{b}_\nu^\dagger \hat{b}_\nu \rangle$, and the correlation $C(\tau)$ behave similarly as in Figs. 4(a) and 4(b) and in Fig. 5(a) for the resonant case, except that (i) $\langle \hat{\sigma}^\dagger \hat{\sigma} \rangle$ oscillates slower for larger I_{las}, and the saturated values are smaller; (ii) $\langle \hat{b}_\nu^\dagger \hat{b}_\nu \rangle$ shows smaller oscillations but becomes much larger for the largest I_{las}; (iii) $C(\tau)$ shows only obvious oscillation for the largest I_{las}. These differences are partly due to the weaker molecule near-field coupling, which can be attributed itself partially to the lower field enhancement, and partially to the laser-molecule off-resonance condition.

Figure 6(a) shows different spectra in the blue-detuned case, compared to those in the resonant case as shown in Fig. 5(b). More precisely, the anti-Stokes is almost invisible for the lowest laser intensity I_{las}, which can be attributed partially to the effects mentioned above and partially to the smaller radiation from the NPoM nanocavity at shorter wavelength (due to the off-resonant condition). For moderate $I_{las} = 10^2, 10^3, 10^4$ μW/μm^2, we also observe one peak at around 656 nm additionally to the fluorescence peak at 690 nm. Since this peak evolves to the Mollow side band, we can attribute this peak to the molecule-laser dressed state, which appears under the off-resonant condition for the weak laser intensity. For the largest $I_{las} = 10^5$ μW/μm^2 as considered, both Stokes and anti-Stokes lines remain, while the fluorescence peak disappears and a new peak at laser wavelength $\lambda_{las} = 654$ nm appears. In addition, the Mollow side peaks depart less from λ_{las}, as compared to that in the resonant case for the same laser intensity.

Figures 6(b) and 6(c) show the similar results for the blue-detuned laser illumination as Figs. 4(c) and 5(c) for the resonant laser illumination except that (i) the fluorescence intensity scales first linearly with increasing I_{las} for $I_{las} \leqslant 10$ μW/μm^2; (ii) the Stokes and anti-Stokes lines increase dramatically for $I_{las} \geqslant 10^4$ μW/μm^2, and the Stokes line is

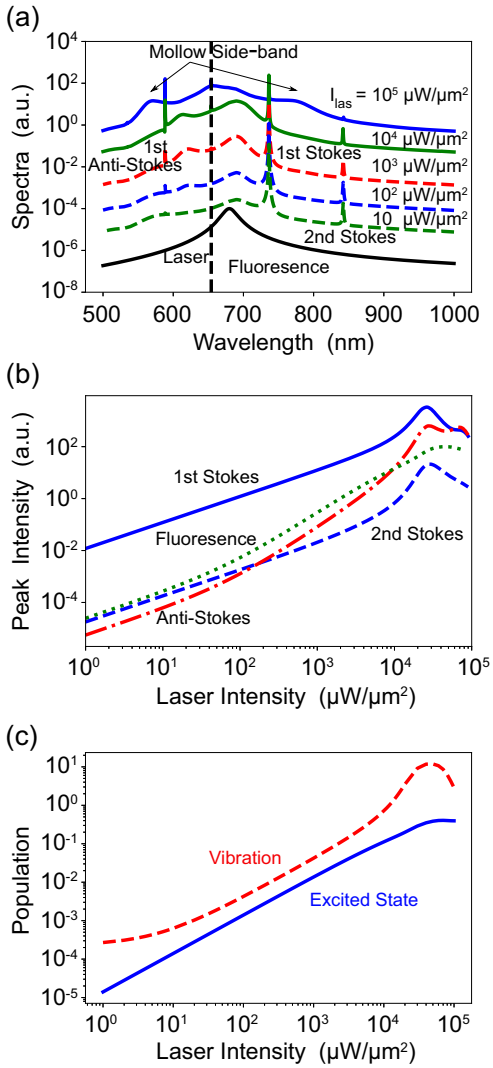

FIG. 6. SERRS response for $\lambda_{las} = 654$ nm laser illumination, which is blue detuned with respect to the Lamb-shifted molecular excitation, and is switched on abruptly at time zero. (a) SERRS spectra for laser intensity $I_{las} = 10, 10^2, 10^3, 10^4, 10^5$ μW/μm^2 (lower to upper curves) and fluorescence spectrum in free space (black curve). (b) The second- and first-order Stokes line (blue dashed and solid line), the anti-Stokes line (red dashed-dotted line), and the fluorescence peak (green dotted line) as a function of I_{las}. (c) Electronic excited-state population $\langle\hat{\sigma}^\dagger\hat{\sigma}\rangle$ and the vibrational population $\langle\hat{b}_\nu^\dagger\hat{b}_\nu\rangle$ for the steady-state system as a function of I_{las}. Other parameters are the same as in Fig. 4.

always stronger than the fluorescence signal, as well as the anti-Stokes line overtakes also the fluorescence signal for larger I_{las}; (iii) the vibrational population $\langle\hat{b}_\nu^\dagger\hat{b}_\nu\rangle$ increases gradually from the thermal value $n_\nu^{th} = 2.29 \times 10^{-4}$ for small laser intensity $I_{las} \leqslant 10$ μW/μm^2, and it increases dramatically over about 10 for $I_{las} \geqslant 10^4$ μW/μm^2, much larger than that in the resonant case; (iv) the electronic excited-state population $\langle\hat{\sigma}^\dagger\hat{\sigma}\rangle$ reaches the constant value 0.5 for $I_{las} \approx 2 \times 10^4$ μW/μm^2, and it is smaller than $\langle\hat{b}_\nu^\dagger\hat{b}_\nu\rangle$ for all I_{las}.

The dramatic increase of the vibrational population and the Raman signal at $I_{las} \geqslant 10^4$ μW/μm^2 are due to the stimulated vibrational excitation, which is similar to the stimulated emission in laser operation, and is known as phonon lasing or parametric instability in cavity and molecular optomechanics [9,11]. However, this dramatic increase is limited finally by the suppressed Raman scattering due to the two-level nature of the molecular electronic excitation.

In Figs. 8(c) and 8(d) of Appendix C, we have further examined the evolution of the Raman line shape for the blue-detuned laser illumination, and found that for the relatively weak laser illumination, (i) the Raman shift of the first-order Stokes lines and anti-Stokes line increase and decrease with same magnitude, respectively, and the increase of the Raman shift of the second-order Stokes line is about twice larger; (ii) the linewidth of the Raman lines reduces for sufficiently larger laser intensity. In addition, for stronger laser illumination, the behavior of Raman shift reverses, and the Raman linewidth shows two minima. These behaviors are consistent with the changes of the vibrational population.

C. Red-detuned laser excitation

In this sub-section, we complete our analysis by examining in Fig. 7 the system response to the $\lambda_{las} = 736$ nm laser illumination, which is red detuned with respect to the molecular excitation. In Figs. 9(d)–9(f) of Appendix C, we show that the change of the population and the two-time correlation are similar to that for laser illumination blue detuned with respect to the molecular excitation.

Figure 7(a) shows similar SERRS spectra as those in Fig. 6(a) for the blue-detuned laser illumination except that (i) the extra broad peak close to the fluorescence peak for moderate I_{las} appears at longer wavelength; (ii) for largest $I_{las} = 10^5$ μW/μm^2 there appear two dips at the Stokes and anti-Stokes wavelengths, i.e., Fano features [23]. Figures 7(b) and 7(c) show a similar change of the spectral intensity and population as in Figs. 6(b) and 6(c) for the blue-detuned laser illumination except (i) the fluorescence and the anti-Stokes line scale linearly with increasing I_{las} for $I_{las} \leqslant 10^2$ μW/μm^2, and they become much larger than the Stokes line for $I_{las} \geqslant 5 \times 10^3$ μW/μm^2; (ii) the vibrational population $\langle\hat{b}_\nu^\dagger\hat{b}_\nu\rangle$ remains constant up to a laser intensity $I_{las} \leqslant 10^2$ μW/μm^2, which is about 10 times larger than the intensity for the blue-detuned illumination, and it saturates at 0.3 for the largest I_{las} considered instead of increasing dramatically.

In comparison to the cases with resonant and blue-detuned laser illumination, the rate of vibrational pumping is much smaller in this case, and this leads to a relatively larger laser intensity to observe the nonlinear anti-Stokes scattering and the vibrational pumping, and to a relatively smaller vibrational population for a given laser intensity. In Figs. 8(e) and 8(f) of Appendix C, we have further examined the evolution of the Raman line shape for the red-detuned laser illumination, and found that the Raman shift of the Stokes and anti-Stokes lines is decreased and increased, respectively, and the linewidth of the Raman lines starts increasing for laser intensity larger than 2×10^2 μW/μm^2.

D. Discussions and conclusions

In summary, we have developed a theory for surface-enhanced resonant Raman scattering (SERRS) by combining

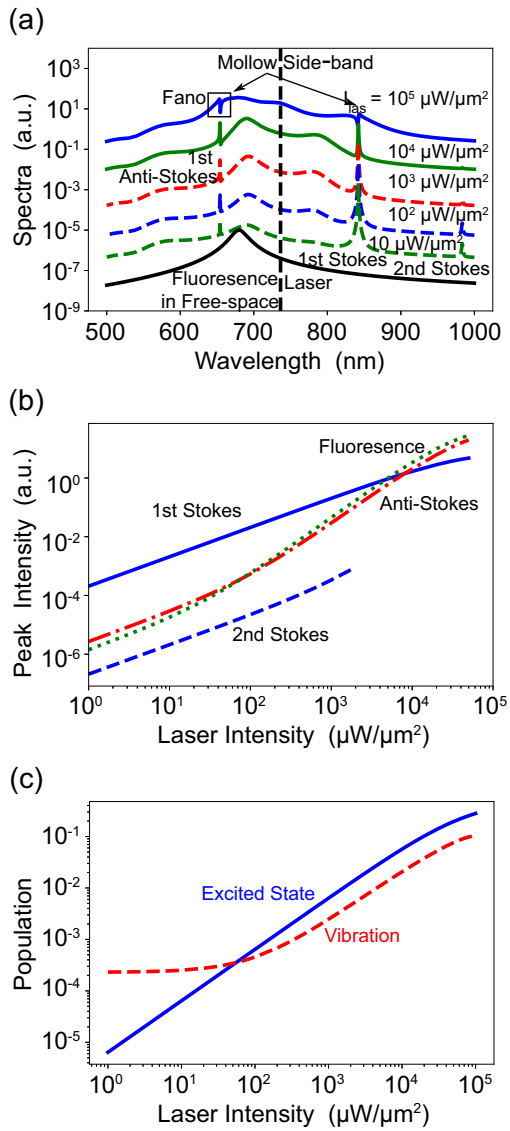

FIG. 7. SERRS response for $\lambda_{las} = 736$ nm laser illumination, which is red detuned with respect to the Lamb-shifted molecular excitation. (a)–(c) Contain the same information at the corresponding panels in Fig. 6.

macroscopic quantum electrodynamics theory [26,27] and electron-vibration interaction in the framework of open quantum system theory, and applied the theory to a realistic system, consisting of a single vertically standing methylene blue molecule inside a gold nanoparticle on mirror (NPoM) nanocavity. From the calculations, we identified a redshift of the molecular excitation of about 40 meV (Lamb shift), and a broadening of the excitation of about 22 meV (Purcell-enhanced decay rate), and a large molecule local field interaction for laser intensities currently available in experiments, which leads to Rabi oscillations, saturated population, and Mollow triplet fluorescence.

Our theory is formally equivalent to molecular optomechanics in the weak-excitation limit, and thus permits many interesting optomechanical effects in SERRS, such as linear scaling of the vibrational population and superlinear scaling of anti-Stokes signal for moderate laser illumination, superlinear scaling of vibrational population and Raman signal for strong blue-detuned laser illumination among other effects, which makes SERRS attractive for exploration of optomechanical effects in experiments. Since electron-vibration coupling is much larger than the typical optomechanical coupling in molecular optomechanics, the laser intensity to observe these effects is expected to be much smaller in SERRS. In addition, we also observe the second-order Stokes line due to the strong electron-vibrational coupling.

Our theory differs from molecular optomechanics in the aspect that the molecule is effectively a two-level system, but the plasmon has infinite levels as a harmonic oscillator. For strong laser excitation, the molecular excitation is saturated, and this leads to the reduction or even the disappearance of the Raman lines. Such behavior might provide an explanation to observations in chemical mapping experiments based on SERRS [see Fig. 4(d) in the supporting information of Ref. [49]] and in nonlinear resonant Stokes Raman scattering experiments with a MoS_2 monolayer inside a NPoM nanocavity (see Fig. 4 of Ref. [50]).

In this study, we have focused on a single vibrational mode and the double resonance of the plasmon and the molecular excitation. Future studies including more vibrational modes and plasmon-molecular excitation detuning [51–53] might reveal more interesting phenomena, such as the Raman overtones. The theory proposed here is valid for a system in the weak coupling regime, as for a single methylene blue molecule in a NPoM nanocavity, but could be further developed for a system in the strong coupling regime, as for many methylene blue molecules in a NPoM nanocavity. In the latter case, we expect to observe novel and interesting physics [22,50,54] due to the formation of plexcitons, i.e., molecule-plasmon dressed states.

We have also found that TDDFT calculations for the methylene blue overestimate the transient dipole moment and the Huang-Rhys factors. Thus, the electronic-vibronic couplings obtained at TDDFT level are much larger than those found in the literature for molecules similar to methylene blue. In the future, more precise calculations of the molecular electronic excited states should be carried out to improve the prediction of the SERRS response.

To conclude, we indicate possible advances of our theory in other aspects if they become significant or necessary for some particular molecules. First, we might consider anharmonic potential energy surface (PES) to account for the anharmonicity-induced vibrational frequency shift. Second, we might assume different curvatures for the PES of the electronic ground and excited states to account for the different vibrational frequencies for molecules on these states. Finally, we might consider higher excited states of molecules to account for their effect on the SERRS. In any case, the current study establishes a good starting point to investigate the rich physics involved in the nanocavity-enhanced SERRS of a single molecule under strong laser illumination.

ACKNOWLEDGMENTS

We thank Ruben Esteban for the insightful discussions. This work is supported by the Projects No. 12004344 and No.

21902148 from the National Nature Science Foundation of China, joint Project No. 21961132023 from the NSFC-DPG, Project No. PID2019-107432GB-I00 from the Spanish Ministry of Science and Innovation, and Grant No. IT1526-22 for consolidated groups of the Basque University, through the Department of Education, Research, and Universities of the Basque Government. The calculations with MATLAB and GAUSSIAN 16 were performed with the supercomputer at the Henan Supercomputer Center.

Y.Z. devised the theory. X.-M.S. and Y.Z. contributed equally to this work. All the authors contributes to the writing of the manuscript.

APPENDIX A: EFFECTIVE MASTER EQUATION FOR MOLECULE

In this Appendix, we derive the effective quantum master equation for a single molecule coupled to the quantized electromagnetic field of the metallic nanostructure. According to macroscopic quantum electrodynamics theory [26,27], the electromagnetic (plasmonic) field can be described as a continuum via the Hamiltonian

$$\hat{H}_f = \int d\mathbf{r} \int_0^\infty d\omega_f \hbar\omega_f \hat{\mathbf{f}}^\dagger(\mathbf{r},\omega_f)\cdot\hat{\mathbf{f}}(\mathbf{r},\omega_f) \tag{A1}$$

with frequency ω_f, creation $\hat{\mathbf{f}}^\dagger(\mathbf{r},\omega_f)$, and annihilation $\hat{\mathbf{f}}(\mathbf{r},\omega_f)$ noise (bosonic) operators at position $\mathbf{r}$, and the quantized electric field operator reads as

$$\hat{\mathbf{E}}(\mathbf{r},\omega_f) = i\sqrt{\frac{\hbar}{\pi\epsilon_0}}\frac{\omega_f^2}{c^2}\int d\mathbf{r}'\sqrt{\epsilon^I(\mathbf{r}',\omega_f)} \times \overleftrightarrow{G}(\mathbf{r},\mathbf{r}';\omega_f)\cdot\hat{\mathbf{f}}(\mathbf{r}',\omega_f), \tag{A2}$$

with the imaginary part of the dielectric function $\epsilon^I(\mathbf{r}',\omega)$ and the classical dyadic Green's function $\overleftrightarrow{G}(\mathbf{r},\mathbf{r}';\omega)$.

We consider the ground and excited electronic states of the molecule, and model them as a two-level system or pseudospins, through the Hamiltonian $\hat{H}_{ele} = \hbar(\omega_e/2)\hat{\sigma}^z$, with intrinsic transition frequency ω_e and the Pauli operator $\hat{\sigma}^z$. In the rotating-wave approximation, the molecule interacts with the quantized electric field via the Hamiltonian $\hat{H}_{fm} = -[\hat{\sigma}^\dagger\mathbf{d}_m\cdot\hat{\mathbf{E}}(\mathbf{r}_m) + \mathbf{d}_m^*\cdot\hat{\mathbf{E}}^\dagger(\mathbf{r}_m)\hat{\sigma}]$, where $\hat{\mathbf{E}}(\mathbf{r}_m) = \int_0^\infty d\omega_f\hat{\mathbf{E}}(\mathbf{r}_m,\omega_f)$ is the sum of the field operator given by Eq. (A2) for all the frequencies ω_f, and $\hat{\sigma}$, $\hat{\sigma}^\dagger$, $\mathbf{d}_m$ are the lowing and raising operators as well as the transition dipole moment of the molecule.

To reduce the degrees of freedom under consideration, we will treat the electromagnetic field as a reservoir and obtain an effective master equation for the molecule by adiabatically eliminating the reservoir degree of freedom. To this end, we first consider the Heisenberg equation for the operator $\hat{o}$ of the molecule:

$$\frac{\partial}{\partial t}\hat{o}(t) = \left[\hat{\sigma}^\dagger(t),\hat{o}(t)\right]\int_0^\infty d\omega_f\frac{\omega_f^2}{c^2}\int d\mathbf{r}' \times\sqrt{\frac{\epsilon^I(\mathbf{r}',\omega_f)}{\hbar\pi\epsilon_0}}\mathbf{d}_m\cdot\overleftrightarrow{G}\left(\mathbf{r}_m,\mathbf{r}';\omega_f\right)\cdot\hat{\mathbf{f}}\left(\mathbf{r}',\omega_f,t\right) - \mathbf{d}_m^*\cdot\int_0^\infty d\omega_f\frac{\omega_f^2}{c^2}\int d\mathbf{r}'\sqrt{\frac{\epsilon^I(\mathbf{r}',\omega_f)}{\hbar\pi\epsilon_0}}\overleftrightarrow{G}^*\cdot (\mathbf{r},\mathbf{r}';\omega_f)\hat{\mathbf{f}}^\dagger(\mathbf{r}',\omega_f,t)[\hat{\sigma}(t),\hat{o}(t)]. \tag{A3}$$

This equation depends on the field operators $\hat{\mathbf{f}}(\mathbf{r}',\omega_f,t)$ [and its conjugation $\hat{\mathbf{f}}^\dagger(\mathbf{r}',\omega_f,t)$], which follows the following Heisenberg equation:

$$\frac{\partial}{\partial t}\hat{\mathbf{f}}(\mathbf{r},\omega_f,t) = -i\omega_f\hat{\mathbf{f}}(\mathbf{r},\omega_f,t) + \frac{\omega_f^2}{c^2}\sqrt{\frac{\epsilon^I(\mathbf{r},\omega_f)}{\hbar\pi\epsilon_0}}\mathbf{d}_m^*\cdot \overleftrightarrow{G}^*(\mathbf{r}_m,\mathbf{r};\omega_f)\hat{\sigma}(t), \tag{A4}$$

where we have used the commutation relations $[\hat{\mathbf{f}}(\mathbf{r}',\omega_f',t),\hat{\mathbf{f}}(\mathbf{r},\omega_f,t)] = 0$ and $[\hat{\mathbf{f}}^\dagger(\mathbf{r}',\omega_f',t),\hat{\mathbf{f}}(\mathbf{r},\omega_f,t)] = -\delta(\mathbf{r}-\mathbf{r}')\delta(\omega_f-\omega_f')$. The formal solution of Eq. (A4) is

$$\hat{\mathbf{f}}(\mathbf{r},\omega_f,t) = \frac{\omega_f^2}{c^2}\sqrt{\frac{\epsilon^I(\mathbf{r},\omega_f)}{\hbar\pi\epsilon_0}}\mathbf{d}_m^*\cdot\overleftrightarrow{G}^*(\mathbf{r}_m,\mathbf{r};\omega_f) \times\int_0^t dt' e^{-i\omega_f(t-t')}\hat{\sigma}(t'). \tag{A5}$$

The equation for the conjugate field operator $\hat{\mathbf{f}}^\dagger(\mathbf{r},\omega_f,t)$ and its formal solution can be achieved by taking the conjugation over Eqs. (A4) and (A5).

At this point, if we insert Eq. (A5) into (A3), we will obtain an integrodifferential equation. By solving this equation, we are able to study not only the Markov dynamics in the weak coupling regime, but also the non-Markov dynamics in the strong coupling regime. Since here we focus on the former regime, we carry out the Born-Markov approximation to the formal solution (A5). To do so, we replace $\hat{\sigma}(t')$ by $e^{i\omega(t-t')}\hat{\sigma}(t)$ in this expression, and then define a new variable $\tau = t-t'$ to change the integration over time, and finally change the upper limit of the integration into infinity to achieve the following expression:

$$\hat{\mathbf{f}}(\mathbf{r},\omega_f,t) \approx \frac{\omega_f^2}{c^2}\sqrt{\frac{\epsilon^I(\mathbf{r},\omega_f)}{\hbar\pi\epsilon_0}}\mathbf{d}_m^*\cdot\overleftrightarrow{G}^*(\mathbf{r}_m,\mathbf{r};\omega_f) \times\hat{\sigma}(t)\left(\pi\delta(\omega-\omega_f)+i\mathcal{P}\frac{1}{\omega-\omega_f}\right). \tag{A6}$$

In the last step, we have utilized the relationship

$$\int_0^\infty d\tau\, e^{i(\omega-\omega_f)\tau} = \pi\delta(\omega-\omega_f)+i\mathcal{P}\frac{1}{\omega-\omega_f}, \tag{A7}$$

where the symbol $\mathcal{P}$ denotes the principal value. Inserting Eq. (A6) (and its conjugation) into Eq. (A3), using the property of the dyadic Green's function

$$\mathrm{Im}G_{k'k}(\mathbf{r}_1,\mathbf{r}_2;\omega_f) = \frac{\omega_f^2}{c^2}\sum_j\int d^3\mathbf{r}'\epsilon^I(\mathbf{r}',\omega_f) \times G_{k'j}(\mathbf{r}_1,\mathbf{r}';\omega_f)G_{kj}^*(\mathbf{r}_2,\mathbf{r}';\omega_f), \tag{A8}$$

and applying the Kramer-Kronig relation

$$\mathcal{P}\int d\omega_f \frac{1}{\omega_f-\omega}\frac{\omega_f^2}{c^2}\mathbf{d}_m\cdot \mathrm{Im}\overleftrightarrow{G}(\mathbf{r}_m,\mathbf{r}_m;\omega_f)\cdot\mathbf{d}_m^* = \pi\frac{\omega^2}{c^2}\mathbf{d}_m\cdot \mathrm{Re}\overleftrightarrow{G}(\mathbf{r}_m,\mathbf{r}_m;\omega)\cdot\mathbf{d}_m^*, \tag{A9}$$

we obtain the following effective master equation:

$$\frac{\partial}{\partial t}\hat{o}(t) = -i[\hat{\sigma}^\dagger(t),\hat{o}(t)]\hat{\sigma}(t)J^{(1)}(\omega_e) - iJ^{(2)}(\omega_e)\hat{\sigma}^\dagger(\tau)[\hat{\sigma}(t),\hat{o}(t)], \tag{A10}$$

with the spectral densities

$$J^{(1)}(\omega_e) = \frac{1}{\hbar\epsilon_0}\frac{\omega^2}{c^2}\mathbf{d}_m\cdot\overleftrightarrow{G}(\mathbf{r}_m,\mathbf{r}_m;\omega_e)\cdot\mathbf{d}_m^*, \tag{A11}$$

$$J^{(2)}(\omega_e) = \frac{1}{\hbar\epsilon_0}\frac{\omega^2}{c^2}\mathbf{d}_m\cdot\overleftrightarrow{G}^*(\mathbf{r}_m,\mathbf{r}_m;\omega_e)\cdot\mathbf{d}_m^*. \tag{A12}$$

Notice that here we have replaced ω by ω_e.

In the next step, we consider the equation for the expectation value $\mathrm{tr}\{\hat{o}(t)\hat{\rho}\} = \mathrm{tr}\{\hat{o}\hat{\rho}(t)\}$, which can be computed either with the time-dependent operator $\hat{o}(t)$ in the Heisenberg picture (left expression) or in the Schrödinger picture (right expression). Using this relationship and the cyclic property of the trace $\mathrm{tr}\{\hat{a}\hat{b}\} = \mathrm{tr}\{\hat{b}\hat{a}\}$ (for any operator $\hat{a},\hat{b}$), we obtain the equation for the reduced density operator

$$\frac{\partial}{\partial t}\hat{\rho} = -i[\hat{\sigma}\hat{\rho},\hat{\sigma}^\dagger]J^{(1)}(\omega_e) - iJ^{(2)}(\omega_e)[\hat{\rho}\hat{\sigma}^\dagger,\hat{\sigma}].$$

Introducing the new parameters

$$\Omega = -\frac{1}{\hbar\epsilon_0}\frac{\omega_e^2}{c^2}\mathbf{d}_m\cdot\mathrm{Re}\overleftrightarrow{G}(\mathbf{r}_m,\mathbf{r}_m;\omega_e)\cdot\mathbf{d}_m^*, \tag{A13}$$

$$\Gamma = \frac{2}{\hbar\epsilon_0}\frac{\omega_e^2}{c^2}\mathbf{d}_m\cdot\mathrm{Im}\overleftrightarrow{G}(\mathbf{r}_m,\mathbf{r}_m;\omega_e)\cdot\mathbf{d}_m^*, \tag{A14}$$

we can rewrite the spectral densities as $J^{(1)}(\omega_e) = -\Omega + i\Gamma/2, J^{(2)}(\omega_e) = -\Omega - i\Gamma/2$. Inserting these expressions into Eq. (A13), we achieve the following effective master equation:

$$\frac{\partial}{\partial t}\hat{\rho} = -i\frac{1}{2}(\omega_e+\Omega)[\hat{\sigma}^z,\hat{\rho}] + \frac{1}{2}\Gamma(2\hat{\sigma}\hat{\rho}\hat{\sigma}^\dagger - \hat{\sigma}^\dagger\hat{\sigma}\hat{\rho} - \hat{\rho}\hat{\sigma}^\dagger\hat{\sigma}). \tag{A15}$$

On the basis of this equation, we arrive at Eq. (1) in the main text where we include the coupling with the local electric field, the Hamiltonian of the vibrational modes, the electron-vibration coupling as well as the other dissipative processes related to the electronic states and the vibrational modes.

APPENDIX B: FAR-FIELD SPECTRUM

In this Appendix, we present the derivation of the far-field radiation from the single molecule in the NPoM nanocavity. According to Ref. [32], the far-field spectrum can be computed with

$$\frac{dW}{d\Omega}(\omega) = \frac{c\epsilon_0 r^2}{4\pi^2}\mathrm{Re}\int_0^\infty d\tau\, e^{i\omega\tau}\mathrm{tr}\{\hat{\mathbf{E}}^\dagger(\mathbf{r}_d,0)\cdot\hat{\mathbf{E}}(\mathbf{r}_d,\tau)\hat{\rho}\}. \tag{B1}$$

In this expression, r is the distance between the molecule and the detector, $\hat{\mathbf{E}}(\mathbf{r},\tau) = \int_0^\infty d\omega_f\hat{\mathbf{E}}(\mathbf{r},\omega_f,\tau)$ is the electric field operator at the detector position $\mathbf{r}_d$, and ω is the frequency of the spectrum. Inserting Eq. (A6) into Eq. (A2), we obtain the expression

$$\hat{\mathbf{E}}(\mathbf{r},\omega_f,\tau) = i\frac{\hbar}{\pi\epsilon_0}\frac{\omega_f^2}{c^2}\mathrm{Im}\overleftrightarrow{G}(\mathbf{r},\mathbf{r}_m;\omega_f)\cdot\mathbf{d}_m^* \times\hat{\sigma}(\tau)\left(\pi\delta(\omega_f-\omega)+i\mathcal{P}\frac{1}{\omega-\omega_f}\right). \tag{B2}$$

Here, we have utilized the relation (A8), and replaced ω by ω_f. Using the above expression and Eq. (A9), we obtain the following expression for the electric field operator:

$$\hat{\mathbf{E}}(\mathbf{r},\tau) = \frac{\hbar}{\epsilon_0}\frac{\omega^2}{c^2}\overleftrightarrow{G}(\mathbf{r},\mathbf{r}_m;\omega)\cdot\mathbf{d}_m^*\hat{\sigma}(\tau). \tag{B3}$$

Applying the conjugation to the above equation, we can obtain the expression for the conjugated field operators $\hat{\mathbf{E}}^\dagger(\mathbf{r},\tau)$. Inserting these results into Eq. (B1), we can rewrite the spectrum as

$$\frac{dW}{d\Omega}(\omega) \approx K(\omega)\mathrm{Re}\int_0^\infty d\tau\, e^{i\omega\tau}\mathrm{tr}\{\hat{\sigma}^\dagger(0)\hat{\sigma}(\tau)\hat{\rho}\} \tag{B4}$$

with the propagation factor

$$K(\omega) = \frac{\hbar^2cr^2}{4\pi^2\epsilon_0}\left|\frac{\omega^2}{c^2}\overleftrightarrow{G}(\mathbf{r},\mathbf{r}_m;\omega)\cdot\mathbf{d}_m^*\right|^2. \tag{B5}$$

To compute the spectrum with Eq. (B4), we need to evaluate the two-time correlations $\mathrm{tr}\{\hat{\sigma}^\dagger(0)\hat{\sigma}(\tau)\hat{\rho}\}$, where τ refers the difference of time with respect to the steady state labeled as "0." To compute these correlations, we consider a pure quantum system. In this case, we can introduce the time-dependent propagation operator $\hat{U}(\tau)$ to reformulate the correlations as

$$\mathrm{tr}\{\hat{\sigma}^\dagger(0)\hat{\sigma}(\tau)\hat{\rho}\} = \mathrm{tr}\{\hat{\sigma}^\dagger\hat{U}^\dagger(\tau)\hat{\sigma}\hat{U}(\tau)\hat{\rho}\} = \mathrm{tr}\{\hat{\sigma}\hat{U}(\tau)\hat{\rho}\hat{\sigma}^\dagger\hat{U}^\dagger(\tau)\} = \mathrm{tr}\{\hat{\sigma}\hat{\varrho}(\tau)\}, \tag{B6}$$

where we have defined the operator $\hat{\varrho}(\tau) = \hat{U}(\tau)\hat{\rho}\hat{\sigma}^\dagger\hat{U}^\dagger(\tau)$. In essence, we have transformed the expression in the Heisenberg picture to that in the Schrödinger picture. To deal with the quantum system in the presence of loss, we should replace $\hat{U}(\tau)\ldots\hat{U}^\dagger(\tau)$ with the time-dependent propagation superoperator $\hat{\mathcal{U}}(\tau)$, which indicates the formal solution of the master equation, such as Eq. (A15). Finally, we can compute the spectrum as

$$\frac{dW}{d\Omega}(\omega) \approx K(\omega)\mathrm{Re}\int_0^\infty d\tau\, e^{i\omega\tau}\mathrm{tr}\{\hat{\sigma}\hat{\varrho}(\tau)\}, \tag{B7}$$

where $\hat{\varrho}(\tau)$ satisfies the same master equation as $\hat{\rho}$, however, with the initial condition $\hat{\varrho}(0) = \hat{\rho}\hat{\sigma}^\dagger$.

APPENDIX C: SUPPLEMENTAL RESULTS

In this Appendix, we present and discuss extra information to supplement the results in the main text.

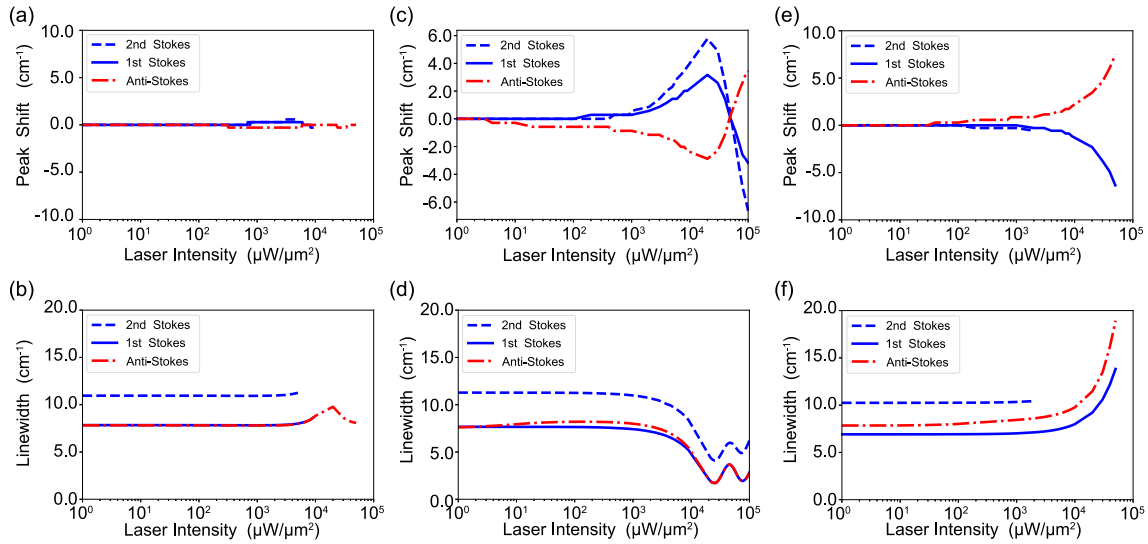

FIG. 8. Evolution of the change of the Raman shift [(a), (c), (e)] and the Raman linewidth [(b), (d), (f)] for laser illumination with increasing laser intensity I_{las} and wavelength $\lambda_{las} = 693$ nm [(a), (b)], $\lambda_{las} = 654$ nm [(c), (d)], $\lambda_{las} = 736$ nm [(e), (f)], which are resonant, blue and red detuned to the Lamb-shifted molecular excitation at 693 nm, respectively. Other parameters are the same as in Fig. 4.

1. Raman peak shift and linewidth variance

In the main text, we have studied how the laser intensity affects the intensity of the Raman peaks. In the following, we provide complement results showing how the laser intensity affects also the frequency and linewidth of the Raman peaks (see Fig. 8).

Figures 8(a) and 8(b) show the change of Raman line shape for laser illumination of increasing intensity I_{las}, which is resonant to the molecular excitation. We see that the frequency of the Raman peaks does not change while the linewidth gets broadened for larger I_{las}. In addition, we find that the second-order Stokes line is about twice broader than the first-order Stokes line.

Figures 8(c) and 8(d) show the change of Raman line shape for laser illumination blue detuned with respect to the molecular excitation. Figure 8(c) shows that for the laser intensity below 2×10^4 μW/μm^2 the Raman shift of the Stokes lines is increased, and the shift increase is about twice larger for the second-order Stokes line, while the Raman shift of the anti-Stokes line is decreased and the magnitude of the shift change is comparable to that of the first-order Stokes line. For much larger laser intensity, the Raman shifts of the Stokes and anti-Stokes lines decrease and increase, respectively. Note that the shifts change the sign at the laser intensity 5×10^4 μW/μm^2. Figure 8(d) shows that the linewidth of the Raman lines starts reducing for laser intensity larger than 10^3 μW/μm^2, and reaches two minima at 2×10^4 μW/μm^2 and 7×10^4 μW/μm^2. These changes of the Raman shift and the linewidth are consistent with the evolution of the spectra and the population, as shown in Figs. 5(a) and 5(c).

Figures 8(e) and 8(f) show the change of Raman line shape for laser illumination red detuned with respect to the molecular excitation. Figure 8(e) shows that the Raman shift of the Stokes and anti-Stokes lines is increased and decreased, respectively. Figure 8(f) shows that the linewidth of the Raman lines starts increasing for laser intensity larger than 2×10^2 μW/μm^2.

2. System dynamics under blue- and red-detuned laser illumination

In the main text, we have illustrated the system dynamics under the laser illumination, which is resonant to the molecular excitation. In Fig. 9, we provide the results for the blue- and red-detuned laser illumination conditions.

Figures 9(a)–9(c) show that the dynamics of the electronic excited-state population (a), vibrational population (b), and two-time correlation (c) for 654-nm laser illumination, blue detuned to the molecular excitation, are similar to those for 693-nm laser excitation resonant to the molecular excitation, as shown in Figs. 4(a) and 4(b) and in Fig. 5(a), except (i) the excited-state population is weaker and its oscillation is slower; (ii) the vibrational population is much larger for a given laser intensity.

Figures 9(d)–9(f) show that the dynamics of the electronic excited-state population (d), vibrational population (e), and two-time correlation (f) for 736-nm laser illumination, red detuned to the molecular excitation, are similar to those for 654-nm laser excitation, blue detuned with respect to the molecular excitation, except that the vibrational population is relatively weak for a given laser intensity.

3. System response under pulsed laser illumination

As explained in the main text, many interesting effects occur for strong laser illumination. Since the continuous-wave laser with large intensity might destroy the sample, it is beneficial to consider the picosecond pulsed laser illumination. To describe the system response in this case, we simply assume a time-dependent molecule near-field coupling $v(t) = v_0 e^{-(t-t_0)^2/(2\sigma^2)}$, where the laser pulse envelope follows a Gaussian function with center t_0 and linewidth $\sigma\sqrt{2\ln 2}$. Because the plasmon mode normally has a lifetime around several femtoseconds, the plasmon excitation follows roughly the laser pulse excitation (see Fig. 14 of [20]), and the above simple treatment of the time-dependent effect is justified.

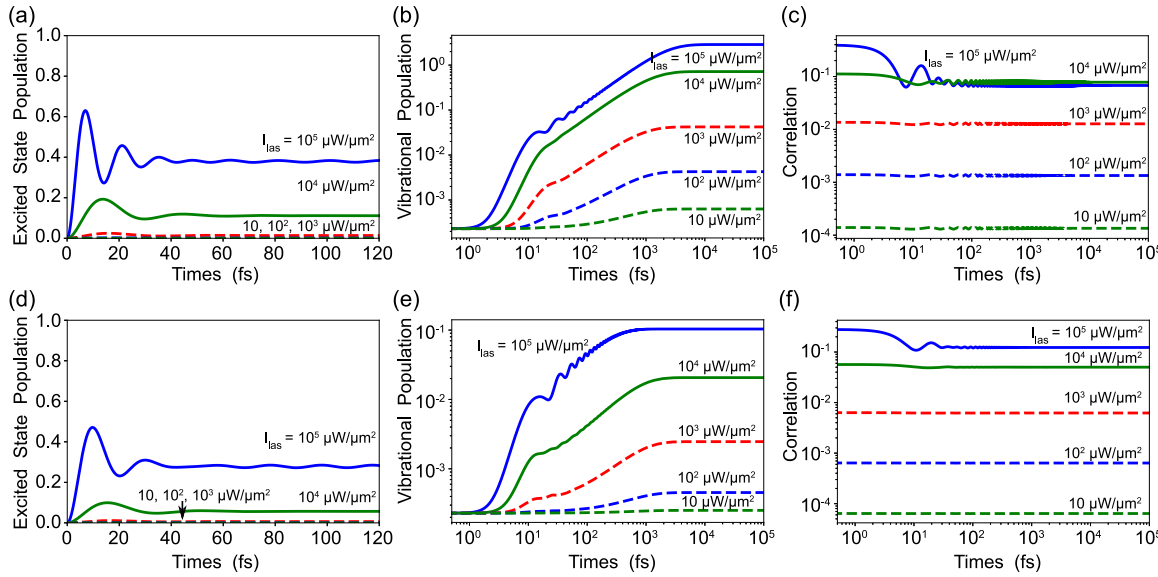

FIG. 9. Electronic excited-state population [(a), (d)], vibrational population [(b), (e)], and two-time correlation [(c), (f)] for the 654-nm [(a)–(c)] and 736-nm [(d)–(f)] laser illumination with increasing intensity I_{las}, which are blue and red detuned to the Lamb-shifted molecular excitation, respectively. Other parameters are the same as in Fig. 4 in the main text.

Figures 10(a) and 10(b) show the evolution of the excited state and vibrational population for the laser pulses resonant to the molecular excitation, which have a center at 1.5 ps, a linewidth of 1 ps, and the increasing intensity from $I_{las} = 10$ μW/μm² to 10^5 μW/μm² (from lower to upper curves).

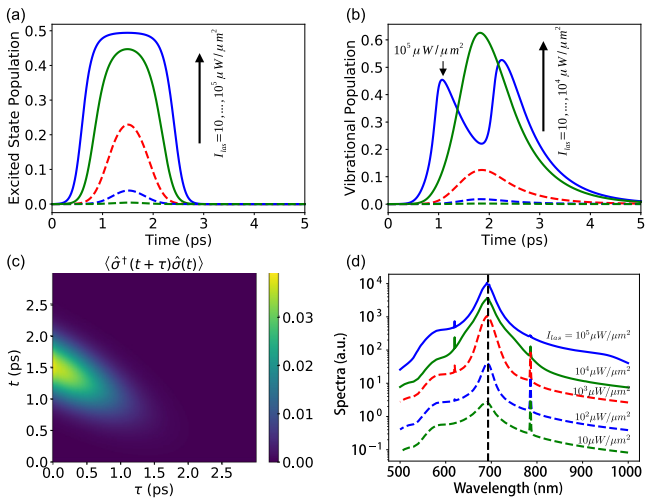

FIG. 10. System response to the pulsed laser illumination with a wavelength $\lambda_{las} = 693$ nm (resonant to the molecular excitation), with a Gaussian shape of center $t_0 = 1.5$ ps and width $2\sqrt{2\ln 2}\sigma = 1$ ps (with σ as standard deviation). (a), (b) Evolution of the excited-state population (a) and the vibrational population (b) for increasing laser intensity $I_{las} = 10, \ldots, 10^5$ μW/μm² (from lower to upper curves). (c) Two-time correlation function $\langle\hat{\sigma}^\dagger(t+\tau)\hat{\sigma}(t)\rangle$ for given laser intensity $I_{las} = 10^2$ μW/μm². (d) The integrated spectrum $dW(\omega)/d\Omega = \int dt\, dW(\omega, t)/d\Omega$ for increasing laser intensity $I_{las} = 10, \ldots, 10^5$ μW/μm² (from bottom to top curves). Note that the intensity of the integrated spectrum can not be directly compared with that for the spectrum under the continuous-wave illumination.

We see that the excited-state population follows the laser pulse shape for weak laser illumination ($I_{las} < 10^4$ μW/μm²), which becomes slightly broader for increasing laser intensity, but becomes flat around 0.5 near the pulse center for the strongest laser illumination ($I_{las} = 10^5$ μW/μm²) due to the saturation effect. At the same time, the vibrational population shows asymmetric shapes with peaks at slightly later time and slow wings for longer time for weak laser illumination ($I_{las} < 10^4$ μW/μm²), but shows one dip around the laser pulse center for strongest laser illumination. The former behavior of the vibration agrees qualitatively with what expected for the molecular optomechanical model (see Fig. 14 of Ref. [20]), while the latter behavior is caused by the population saturation of the electronic excitation.

To investigate the fluorescence and Raman spectra, we introduce the time-dependent spectrum $dW(\omega, t)/d\Omega$, which has similar form as Eq. (B1) except that the steady-state time argument "0" and the Fourier-transform time argument "τ" are replaced by "t" and "$t + \tau$," respectively. Then, following the same derivation as in Appendix B, we arrive at

$$\frac{dW}{d\Omega}(\omega, t) \approx K(\omega)\mathrm{Re}\int_0^\infty d\tau\, e^{-i\omega\tau}\langle\hat{\sigma}^\dagger(\tau + t)\hat{\sigma}(t)\rangle. \quad \text{(C1)}$$

This expression is similar as Eq. (B4) except that we take the complex conjugation inside the integral in order to meet the standard formula considered in QUTIP toolkit. By applying the quantum regression theorem, we have calculated the two-time correlation for the resonant laser illumination with given intensity [Fig. 10(c)], and then the integrated spectrum $dW(\omega)/d\Omega = \int dt\, dW(\omega, t)/d\Omega$ for increasing laser intensity [Fig. 10(d)]. We see that the correlation function at $\tau = 0$ shows a peak around $t = 1.5$ ps, which is equivalent to the

excited-state population $\langle\hat{\sigma}^{\dagger}(t)\hat{\sigma}(t)\rangle$, and the peak shifts to earlier time t with reducing amplitude for increasing time τ. The integrated spectra for the picosecond laser illumination show the similar features as those for the continuous-wave laser illumination [cf. Fig. 5(b)] except that the anti-Stokes lines are relatively weak and the second Stokes lines are invisible. These differences can be attributed to the relatively weak vibrational pumping, and can be improved with longer laser pulses. Thus, we expect that most of the nonlinear behaviors of the Raman scattering and fluorescence, as discussed in the main text, can be still observed with the picosecond laser illumination.

[1] E. C. Le Ru and P. G. Etchegoin, *Principles of Surface-Enhanced Raman Spectroscopy* (Elsevier, Amsterdam, 2009).

[2] J. R. Lombardi, R. L. Birke, T. Lu, and J. Xu, Charge-transfer theory of surface enhanced raman spectroscopy: Herzberg-teller contributions, J. Chem. Phys. **84**, 4174 (1986).

[3] M. Moskovits, Surface-enhanced spectroscopy, Rev. Mod. Phys. **57**, 783 (1985).

[4] H. Xu, J. Aizpurua, M. Käll, and P. Apell, Electromagnetic contributions to single-molecule sensitivity in surface-enhanced raman scattering, Phys. Rev. E **62**, 4318 (2000).

[5] K. Kneipp, Y. Wang, H. Kneipp, I. Itzkan, R. R. Dasari, and M. S. Feld, Population Pumping of Excited Vibrational States by Spontaneous Surface-Enhanced Raman Scattering, Phys. Rev. Lett. **76**, 2444 (1996).

[6] R. C. Maher, P. G. Etchegoin, E. C. Le Ru, and L. F. Cohen, A Conclusive demonstration of vibrational pumping under surface enhanced raman scattering conditions, J. Phys. Chem. B **110**, 11757 (2006).

[7] R. C. Maher, C. M. Galloway, E. C. Le Ru, L. F. Cohen, and P. G. Etchegoin, Vibrational pumping in surface enhanced raman scattering (SERS), Chem. Soc. Rev. **37**, 965 (2008).

[8] C. M. Galloway, E. C. Le Ru, and P. G. Etchegoin, Single-molecule vibrational pumping in SERS, Phys. Chem. Chem. Phys. **11**, 7372 (2009).

[9] M. K. Schmidt, R. Esteban, A. González-Tudela, G. Giedke, and J. Aizpurua, Quantum mechanical description of raman scattering from molecules in plasmonic cavities, ACS Nano **10**, 6291 (2016).

[10] P. Roelli, C. Galland, N. Piro, and T. J. Kippenberg, Molecular cavity optomechanics as a theory of plasmon-enhanced raman scattering, Nat. Nanotechnol. **11**, 164 (2016).

[11] M. Aspelmeyer, T. J. Kippenberg, and F. Marquardt, Cavity optomechanics, Rev. Mod. Phys. **86**, 1391 (2014).

[12] M. K. Schmidt, R. Esteban, F. Benz, J. J. Baumberg, and J. Aizpurua, Linking classical and molecular optomechanics descriptions of SERS, Faraday Discuss. **205**, 31 (2017).

[13] Y. Zhang, J. Aizpurua, and R. Esteban, Optomechanical collective effects in surface-enhanced raman scattering from many molecules, ACS Photonics **7**, 1676 (2020).

[14] M. K. Dezfouli, R. Gordon, and S. Hughes, Molecular optomechanics in the anharmonic cavity-qed regime using hybrid metal-dielectric cavity modes, ACS Photonics **6**, 1400 (2019).

[15] W. M. Deacon, Y. Zhang, L. A. Jakob, E. Pavlenko, S. Hu, C. Carnegie, T. Neuman, R. Esteban, J. Aizpurua, and J. J. Baumberg, Softening molecular bonds through the giant optomechanical spring effect in plasmonic nanocavities, arXiv:2204.09641.

[16] W. Zhu and K. B. Crozier, Quantum mechanical limit to plasmonic enhancement as observed by surface-enhanced raman scattering, Nat. Commun. **5**, 5228 (2014).

[17] J. J. Baumberg, J. Aizpurua, M. H. Mikkelsen, and D. R. Smith, Extreme nanophotonics from ultrathin metallic gaps, Nat. Mater. **18**, 668 (2019).

[18] X. Wang, S.-C. Huang, T.-X. Huang, H.-S. Su, J.-H. Zhong, Z.-C. Zeng, M.-H. Li, and B. Ren, Tip-enhanced raman spectroscopy for surfaces and interfaces, Chem. Soc. Rev. **46**, 4020 (2017).

[19] F. Benz, M. K. Schmidt, A. Dreismann, R. Chikkaraddy, Y. Zhang, A. Demetriadou, C. Carnegie, H. Ohadi, B. De Nijs, R. Esteban, J. Aizpurua, and J. J. Baumberg, Single-molecule optomechanics in "picocavities", Science **354**, 726 (2016).

[20] A. Lombardi, M. K. Schmidt, L. Weller, W. M. Deacon, F. Benz, B. de Nijs, J. Aizpurua, and J. J. Baumberg, Pulsed Molecular Optomechanics in Plasmonic Nanocavities: From Nonlinear Vibrational Instabilities to Bond-Breaking, Phys. Rev. X **8**, 011016 (2018).

[21] Y. Xu, H. Hu, W. Chen, P. Suo, Y. Zhang, S. Zhang, and H. Xu, Phononic cavity optomechanics of atomically thin crystal in plasmonic nanocavity, ACS Nano **16**, 12711 (2022).

[22] T. Neuman, J. Aizpurua, and R. Esteban, Quantum theory of surface-enhanced resonant raman scattering (SERRS) of molecules in strongly coupled plasmon-exciton systems, Nanophotonics **9**, 295 (2020).

[23] T. Neuman, R. Esteban, G. Giedke, M. K. Schmidt, and J. Aizpurua, Quantum description of surface-enhanced resonant raman scattering within a hybrid-optomechanical model, Phys. Rev. A **100**, 043422 (2019).

[24] Y. Zhang, R. Esteban, R. A. Boto, M. Urbieta, X. Arrieta, C.-X. Shan, S. Li, J. J. Baumberg, and J. Aizpurua, Addressing molecular optomechanical effects in nanocavity-enhanced raman scattering beyond the single plasmonic mode, Nanoscale **13**, 1938 (2021).

[25] A. Delga, J. Feist, J. Bravo-Abad, and F. J. Garcia-Vidal, Quantum Emitters Near a Metal Nanoparticle: Strong Coupling and Quenching, Phys. Rev. Lett. **112**, 253601 (2014).

[26] N. Rivera and I. Kaminer, Light-matter interactions with photonic quasiparticles, Nat. Rev. Phys. **2**, 538 (2020).

[27] S. Scheel and S. Buhmann, Macroscopic quantum electrodynamics-Concepts and applications, Acta Phys. Slovaca **58**, 675 (2008).

[28] R. Chikkaraddy, B. de Nijs, F. Benz, S. J. Barrow, O. A. Scherman, E. Rosta, A. Demetriadou, P. Fox, O. Hess, and J. J. Baumberg, Single-molecule strong coupling at room temperature in plasmonic nanocavities, Nature (London) **535**, 127 (2016).

[29] Y. Zhang, Q.-S. Meng, L. Zhang, Y. Luo, Y.-J. Yu, B. Yang, Y. Zhang, R. Esteban, J. Aizpurua, Y. Luo, J.-L. Yang, Z.-C. Dong, and J. G. Hou, Sub-nanometre control of the coherent interaction between a single molecule and a plasmonic nanocavity, Nat. Commun. **8**, 15225 (2017).

[30] B. Yang, G. Chen, A. Ghafoor, Y. Zhang, Y. Zhang, Y. Zhang, Y. Luo, J. Yang, V. Sandoghdar, J. Aizpurua, Z. C. Dong, and J. G. Hou, Sub-nanometre resolution in single-molecule photoluminescence imaging, Nat. Photonics **14**, 693 (2020).

[31] S. Y. Lyu, Y. Zhang, Y. Zhang, K. Chang, G. Zheng, and L. X. Wang, Picocavity-controlled subnanometer-resolved single-molecule fluorescence imaging and mollow triplets, J. Phys. Chem. C **126**, 11129 (2022).

[32] M. O. Scully and M. S. Zubairy, *Quantum Optics* (Cambridge University Press, Cambridge, 1997).

[33] H. P. Breuer and F. Petruccione, *The Theory of Open Quantum Systems* (Clarendon, Oxford, 2007).

[34] K. Huang and A. Rhys, Theory of light absorption and non-radiative transitions in F-centres, Proc. R. Soc. A **204**, 406 (1950).

[35] J. R. Johansson, P. D. Nation, and F. Nori, QuTiP: An open-source python framework for the dynamics of open quantum systems, Comput. Phys. Commun. **183**, 1760 (2012).

[36] J. R. Johansson, P. D. Nation, and F. Nori, QuTiP 2: A Python framework for the dynamics of open quantum systems, Comput. Phys. Commun. **184**, 1234 (2013).

[37] T. Holstein and H. Primakoff, Field dependence of the intrinsic domain magnetization of a ferromagnet, Phys. Rev. **58**, 1098 (1940).

[38] S. Hirata and M. Head-Gordon, Time-dependent density functional theory within the tamm-dancoff approximation, Chem. Phys. Lett. **314**, 291 (1999).

[39] Y. Hu, C.-W. Wang, C. Zhu, F. Gu, and S.-H. Lin, Franck-Condon simulation for unraveling vibronic origin in solvent enhanced absorption and fluorescence spectra of rubrene, RSC Advances **7**, 12407 (2017).

[40] F. Duschinsky, The importance of the electron spectrum in multi atomic molecules. Concerning the Franck-Condon principle, Acta Physicochim. URSS **7**, 551 (1937).

[41] T. Neuman, R. Esteban, D. Casanova, F. J. García-Vidal, and J. Aizpurua, Coupling of molecular emitters and plasmonic cavities beyond the point-dipole approximation, Nano Lett. **18**, 2358 (2018).

[42] T. B. de Queiroz, E. R. de Figueroa, M. D. Coutinho-Neto, C. D. Maciel, E. Tapavicza, Z. Hashemi, and L. Leppert, First principles theoretical spectroscopy of methylene blue: between limitations of time-dependent density functional theory approximations and its realistic description in the solvent, J. Chem. Phys. **154**, 044106 (2021).

[43] F. J. García de Abajo, Optical excitations in electron microscopy, Rev. Mod. Phys. **82**, 209 (2010).

[44] F. J. García de Abajo and A. Howie, Retarded field calculation of electron energy loss in inhomogeneous dielectrics, Phys. Rev. B **65**, 115418 (2002).

[45] U. Hohenester and A. Trügler, MNPBEM - A matlab toolbox for the simulation of plasmonic nanoparticles, Comput. Phys. Commun. **183**, 370 (2012).

[46] J. Waxenegger, A. Trügler, and U. Hohenester, Plasmonics simulations with the MNPBEM toolbox: Consideration of substrates and layer structures, Comput. Phys. Commun. **193**, 138 (2015).

[47] P. B. Johnson and R. W. Christy, Optical constants of the noble metals, Phys. Rev. B **6**, 4370 (1972).

[48] G. W. Ford and W. H. Weber, Electromagnetic interactions of molecules with metal surfaces, Phys. Rep. **113**, 195 (1984).

[49] R. Zhang, Y. Zhang, Z. C. Dong *et al.*, Chemical mapping of a single molecule by plasmon-enhanced raman scattering, Nature (London) **498**, 82 (2013).

[50] X. Liu, J. Yi, S. Yang *et al.*, Nonlinear valley phonon scattering under the strong coupling regime, Nat. Mater. **20**, 1210 (2021).

[51] F. Benz, R. Chikkaraddy, A. Salmon, H. Ohadi, B. de Nijs, J. Mertens, C. Carnegie, R. W. Bowman, and J. J. Baumberg, SERS of individual nanoparticles on a mirror: Size does matter, but so does shape, J. Phys. Chem. Lett. **7**, 2264 (2016).

[52] Y. Zhang, W. Chen, T. Fu, J. Sun, D. Zhang, Y. Li, S. Zhang, and H. Xu, Simultaneous surface-enhanced resonant raman and fluorescence spectroscopy of monolayer MoS_2: determination of ultrafast decay rates in nanometer dimension, Nano Lett. **19**, 6284 (2019).

[53] R. B. Jaculbia, H. Imada, K. Miwa, T. Iwasa, M. Takenaka, B. Yang, E. Kazuma, N. Hayazawa, T. Taketsugu, and Y. Kim, Single-molecule resonance raman effect in a plasmonic nanocavity, Nat. Nanotechnol. **15**, 105 (2020).

[54] P. A. Thomas, W. J. Tan, H. A. Fernandez, and W. L. Barnes, A new signature for strong light-matter coupling using spectroscopic ellipsometry, Nano Lett. **20**, 6412 (2020).